J. Fluid Mech. (2010), *vol.* 651, *pp.* 1–26. © Cambridge University Press 2010
doi:10.1017/S0022112010000261

Acoustic mode scattering from a heat source

O. V. ATASSI† AND J. J. GILSON

Department of Aerodynamics, Pratt and Whitney, 400 Main Street, East Hartford, CT 06108, USA

(Received 1 August 2009; revised 12 January 2010; accepted 13 January 2010)

The scattering of an incident acoustic wave by a non-uniform mean flow resulting from a heat source is investigated. The heat source produces gradients in the mean flow and the speed of sound that scatter the incident duct acoustic mode into vortical, entropic, and higher-order acoustic modes. Linear solutions utilizing the compact source limit and nonlinear solutions to the Euler equations are computed to understand how variations in the amplitude and axial extent of the heat source as well as the incident acoustic wave propagation angle and amplitude modify the scattered solution. For plane wave excitation, significant entropy waves are produced as the net heat addition increases at the expense of the transmitted acoustic energy. When the net heat addition is held constant, increasing the axial extent of the heat source results in a reduction of the entropy waves produced downstream and a corresponding increase in the downstream scattered acoustic energy. For circumferential acoustic mode excitations the incident acoustic wave angle, characterized by the cutoff ratio, significantly modifies the scattered acoustic energy. As the propagating mode cutoff ratio approaches unity, a rise in the scattered vortical disturbance and a decrease in the entropic disturbance amplitude is observed. As the cutoff ratio increases, the scattered solution approaches the plane wave results. Moreover, incident acoustic waves with different frequencies and circumferential mode orders but similar cutoff ratios yield similar scattered wave coefficients. Finally, for large amplitude incident acoustic waves the scattered solution is modified by nonlinear effects. The pressure field exhibits nonlinear steepening of the wavefront and the nonlinear interactions produce higher harmonic frequency content which distorts the sinusoidal variation of the outgoing scattered acoustic waves.

1. Introduction

In combustors, heat addition generates mean flow gradients which modify the mean flow downstream of the flame zone. Unsteady fluctuations in heat release are produced by velocity perturbations near the flame surface that excite duct acoustic eigenmodes producing noise. When the net gain in acoustic energy from the interaction between the flame and the acoustic duct modes exceeds the energy expelled from the combustion chamber, combustion instability results (Rayleigh 1896). This has led to interest in determining (i) the reflection and transmission of acoustic waves in heated flows and nozzles (Marble & Candel 1977; Stow, Dowling & Hynes 2002) and (ii) computing the local acoustic velocity fluctuations near the flame surface (Dowling 1997). In this paper, we examine these two issues by studying the scattering of

† Email address for correspondence: oliver34@comcast.net

https://doi.org/10.1017/S0022112010000261 Published online by Cambridge University Press

circumferential acoustic waves by a heat source into upstream propagating acoustic waves and downstream propagating vortical, entropic and acoustic waves.

Early studies on the reflection and transmission of acoustic waves in a nozzle utilized the compact nozzle limit (Tsien 1952; Bohn 1977; Marble & Candel 1977; Mani 1981), where the wavelength of the acoustic waves is large relative to the radius of the nozzle. In this limit, only plane waves propagate and the mean flow can be treated as uniform upstream and downstream of a zone of rapid variation. The upstream and downstream solutions can then be related by the Rankine–Hugoniot jump conditions applied at the interface between the two regions. They derived analytical expressions for the reflection and transmission coefficients which depend upon the change in Mach number upstream and downstream of the nozzle throat.

Many combustors are annular in geometry and produce a superposition of circumferentially varying acoustic modes which can be characterized as spinning or standing wave modes (Evesque & Polifke 2002; Evesque, Polifke & Pankiewitz 2003). The transmission and reflection of these modes in annular nozzles can be significantly different from plane waves. Stow *et al.* (2002) extended the plane wave results to consider the scattering of circumferentially-varying modes in the narrow annulus limit for a choked nozzle. They found that besides reflection and transmission of the incident acoustic wave at the throat, scattering of energy into a vorticity and an entropy wave occurred. Subsequent work has analysed the reflection and transmission of one-dimensional flow disturbances over a wider range of frequencies and the impact of shocks on the solutions (Moase, Brear & Manzie (2007); Lamarque & Poinsot 2008).

The effect of non-uniform mean flow and density gradients due to heat addition (Dowling 1995) also has a significant effect on the propagation and scattering of flow disturbances. Density gradients modify the speed of sound and the acoustic duct eigenmodes (Sujith, Waldherr & Zinn 1995; Kim & Williams 1998; Subrahmanyam, Sujith & Lieuwen 2001; Roux *et al.* 2005). Vortical and entropic waves also propagate and their stability can be modified by both the velocity and density gradients leading to large amplitude disturbances and nonlinear steepening (Tyagi & Sujith 2003; Atassi 2007). Karimi, Brear & Moase (2008) considered a one-dimensional heated flow with acoustic and entropic forcing. They found that low-frequency acoustic and entropic excitations generated significant entropic disturbances downstream of the heat source while high-frequency excitations generate little entropy and most of the incident wave energy goes into reflected and transmitted acoustic waves.

The objective of this paper is to examine how in annular geometries acoustic energy is scattered by a heat source into entropic, vortical and acoustic disturbances. To isolate the effect of the heat addition, we first contrast the scattering by a heat source with that in an adiabatic converging nozzle that produces the same rise in Mach number. We then consider (i) the effect of the heat source amplitude and width on the scattering of incident plane and circumferential acoustic modes, (ii) the effect of the cutoff ratio of the incident acoustic wave on the scattered modes and (iii) the amplitude of the incident acoustic wave on the scattered modes. In § 2, we formulate the scattering of incident acoustic waves in an annular duct governed by the Euler equations with a heat source. We first consider the general problem and then the compact source limit where the modes upstream and downstream of the heat source are matched using the Rankine–Hugoniot jump conditions. In § 3, numerical results are presented for the scattering of both plane and circumferential acoustic waves. The numerical cases examine (i) the range of validity of the compact source limit by considering heat source distributions with various widths and acoustic wave excitation

https://doi.org/10.1017/S0022112010000261 Published online by Cambridge University Press

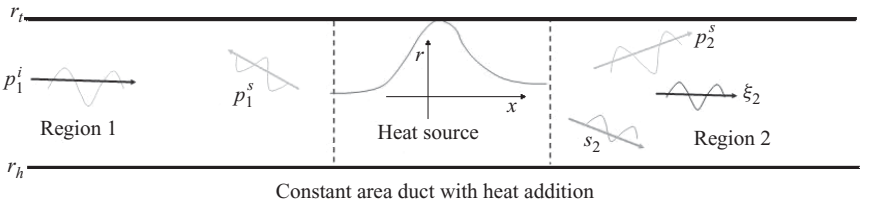


FIGURE 1. Conceptual sketch of annular duct geometry and location of heat source, Q.

at different frequencies and amplitudes and (ii) how well the scattered disturbances of the circumferential modes can be characterized by the cutoff ratio of the incident acoustic mode. Finally, § 4 presents the conclusions of the paper.

2. Mathematical formulation

In this section, we formulate the scattering of an incident acoustic wave by mean flow gradients produced from a heat source. Figure 1 shows a conceptual sketch of the model consisting of a heat source in an annular duct characterized by an inner radius, r_h, and outer radius, r_t. We first present the nonlinear scattering formulation, in § 2.1, where the Euler equations are solved numerically, subject to an imposed incident acoustic wave and a Gaussian heat source, and a local linearization is applied at the nonreflecting inflow/outflow boundary conditions. A simplified linear model which assumes small-amplitude disturbances and examines the low frequency limit is also presented in § 2.2.

2.1. *Nonlinear formulation: sound scattering from a Gaussian heat source*

We model the problem as an inviscid non-heat conducting flow governed by the Euler equations. The conservation equations in the volume, Ω, bounded by the surface, $\partial\Omega$, are expressed as

$$\frac{\partial}{\partial t}\int_{\Omega} \boldsymbol{W}_i \,\mathrm{d}\Omega + \int_{\partial\Omega} \boldsymbol{F}_{ij}^{C} n_j \,\mathrm{d}\Gamma = S_i, \tag{2.1}$$

where n_j is the unit normal of the surface $\partial\Omega$, the vector, $\boldsymbol{W}_i$, and tensor, $\boldsymbol{F}_{ij}^{C}$, are the conservation variables and convective fluxes for mass, momentum and energy, respectively, and the source term, $\boldsymbol{S}_i$, contains a heat source, $\tilde{Q}(\boldsymbol{x})$, in the energy equation. These quantities are given explicitly in Cartesian coordinates as

$$\left.\begin{aligned} \boldsymbol{W}_i &= [\rho\ \rho u\ \rho v\ \rho w\ E]^{\mathrm{T}} \\ \boldsymbol{F}_{ij} &= [\rho u_j\ \ p\delta_{1j} + \rho u u_j\ \ p\delta_{2j} + \rho v u_j\ \ p\delta_{3j} + \rho w u_j\ \ (E+p)u_j]^{\mathrm{T}} \\ \boldsymbol{S}_i &= [0\ 0\ 0\ 0\ \tilde{Q}(\boldsymbol{x},t)]^{\mathrm{T}} \end{aligned}\right\} \tag{2.2}$$

where ρ is the density, $\boldsymbol{u}_j = [u\ \ v\ \ w]^{\mathrm{T}}$ are the Cartesian coordinates of the velocity field, $\boldsymbol{F}_{ij}$ is the jth column of the (5×3) tensor $\boldsymbol{F}_{ij}^{C}$, p is the pressure and $E = \rho(c_v T + 1/2|u|^2)$ is the total internal energy with temperature, T, and specific heat at constant volume, c_v. In general, the imposed compact source can be decomposed into steady and unsteady terms, $\tilde{Q}(\boldsymbol{x},t) = Q(\boldsymbol{x}) + q'(\boldsymbol{x},t)$. In this paper, the imposed compact, steady heat source is Gaussian, $Q(x) = A\exp(-x^2/\sigma^2)$, and is characterized by its amplitude, A and its axial extent, σ. The geometry is an annular duct with outer radius, $r = r_t$ and inner radius, $r = r_h$. At the surface of the duct, $r = r_h, r_t$, and at any solid bodies

https://doi.org/10.1017/S0022112010000261 Published online by Cambridge University Press

which lie in the computational domain, the impermeability condition,

$$\int_{\partial\Omega} u_j n_j \, \mathrm{d}\Gamma = 0, \tag{2.3}$$

is applied. In what follows, we non-dimensionalize all lengths by the outer radius of the duct, r_t, the velocity by the inlet speed of sound, c_1, and the density by the inlet mean density, $\overline{\rho}_1$.

2.1.1. *Inflow/outflow boundary conditions*

At the inflow boundary, an incident acoustic wave, which is a solution to the linearized Euler equations, is imposed. Non-reflecting boundary conditions are then imposed on the scattered solution resulting from the interaction of the incident wave with the mean flow gradients. We assume that the inflow/outflow boundaries are located sufficiently far from the source region where nonlinear effects and vorticity are small such that the flow is approximated by the linearized Euler equations perturbed about a uniform mean flow. In this propagation region, Ω_p, the flow variables are locally decomposed into a sum between their steady mean values and their unsteady disturbances,

$$\left.\begin{aligned} \boldsymbol{v} &= \boldsymbol{U} + \boldsymbol{u}(\boldsymbol{x}, t), \quad \boldsymbol{x} \in \Omega_p, \\ p &= P + p'(\boldsymbol{x}, t), \\ \rho &= \overline{\rho} + \rho'(\boldsymbol{x}, t), \end{aligned}\right\} \tag{2.4}$$

where $\boldsymbol{U} = [M \;\; 0 \;\; 0]$ is the mean velocity field, M is the mean axial Mach number, P is the dimensionless mean pressure, $\overline{\rho}$ is the dimensionless mean density and $\boldsymbol{u}, p'(\boldsymbol{x}, t), \rho'(\boldsymbol{x}, t)$ are the unsteady velocity, pressure and density, respectively. The unsteady quantities are assumed small such that $\{|\boldsymbol{u}|, |p'|, |\rho'|\} \ll \{M_x, P, \overline{\rho}\}$. The pressure field can be represented in terms of annular duct eigenfunction expansions

$$p'(x, r, \theta, t) = \sum_{n=1}^{n=\infty} \sum_{m=-\infty}^{m=\infty} p_{mn}(x, t) \mathrm{e}^{\mathrm{i}m\theta} R_{mn}(r), \tag{2.5}$$

where the Fourier–Bessel coefficient, p_{mn}, is given by

$$p_{mn}(x, t) = \frac{1}{2\pi \Lambda_{mn}} \int_{r_h}^{1} \int_{0}^{2\pi} r \bar{R}_{mn}(r) \mathrm{e}^{-\mathrm{i}m\theta} p'(x, r, \theta, t) \, \mathrm{d}\theta \, \mathrm{d}r, \tag{2.6}$$

where

$$\Lambda_{mn} = \int_{r_h}^{1} r |R_{mn}|^2 \, \mathrm{d}r.$$

The orthogonal eigenfunctions, $R_{mn}(r)$, are a combination of Hankel functions (Courant & Hilbert 1937),

$$R_{mn}(r) = H_m^{(1)}(\lambda_{mn} r) - \frac{\mathrm{d}H_m^{(1)}(\lambda_{mn} r_h)/\mathrm{d}r}{\mathrm{d}H_m^{(2)}(\lambda_{mn} r_h)/\mathrm{d}r} H_m^{(2)}(\lambda_{mn} r), \tag{2.7}$$

where λ_{mn} is the eigenvalue associated with the radial eigenfunction, R_{mn}, and the overbar in (2.6) denotes the complex conjugate. The eigenvalue at the boundary is

https://doi.org/10.1017/S0022112010000261 Published online by Cambridge University Press

determined by the impermeability condition at the hub and tip of the annulus,

$$\begin{vmatrix} H_m^{\prime(1)}(\lambda_{mn} r_h) & H_m^{\prime(2)}(\lambda_{mn} r_h) \\ H_m^{\prime(1)}(\lambda_{mn}) & H_m^{\prime(2)}(\lambda_{mn}) \end{vmatrix} = 0. \tag{2.8}$$

Thus, the normal mode vector of an incident acoustic disturbance is

$$\boldsymbol{Y}_i = \boldsymbol{A}(r) \mathrm{e}^{\mathrm{i}(m\theta + k_{mn}^{+} x - \tilde{\omega} t)}, \tag{2.9}$$

where $\boldsymbol{Y}_i = [p' \; u_x \; u_\theta \; u_r \; \rho']^{\mathrm{T}}$. The circumferential wavenumber m, radial mode order n and reduced frequency $\tilde{\omega} = \Omega r_t / c$ are inputs. In what follows, we drop the tildes for convenience. The axial wavenumber is given by

$$k_{mn}^{\pm} = \frac{\omega \left(-M \pm \sqrt{1 - \left(\dfrac{\beta \lambda_{mn}}{\omega} \right)^2} \right)}{\beta^2}, \tag{2.10}$$

where + (−) indicates modes propagating with a group velocity downstream (upstream) and $\beta = \sqrt{1 - M^2}$ is the Prandtl–Glauert factor. The parameter in the square root, $\omega/(\lambda_{mn}\beta)$, is the cutoff ratio. When it is greater than one, acoustic waves propagate in the duct carrying acoustic energy. When it is less than one, evanescent disturbances decay in the duct. The amplitude vector is

$$\boldsymbol{A}^{\mathrm{T}} = a_{i,a} R_{mn} \left[1, \frac{1}{(\omega/k_{mn}^{+} - M)}, \frac{m/r}{k_{mn}^{+}[(\omega/k_{mn}^{+} - M)]}, \frac{-\mathrm{i} \dfrac{\mathrm{d} \ln (R_{mn})}{\mathrm{d}r}}{k_{mn}^{+}(\omega/k_{mn}^{+} - M)}, 1 \right] \tag{2.11}$$

with $a_{i,a}$ as a constant factor. Note that the non-dimensional speed of sound and density at the inlet is unity. The phase velocity, ω/k_{mn}, depends on the Mach number and the cutoff ratio. Thus the relationship between the pressure and the axial velocity depends on the Mach number and the cutoff ratio. The circumferential velocity has an additional dependence on m/k_{mn}.

To complete the initial-boundary-value problem, inflow/outflow conditions must be specified. In order to focus on the scattering results from the mean heat source, we impose non-reflecting boundary conditions at the boundaries. These non-reflecting boundary conditions have been derived in Atassi & Galan (2008) and the results are briefly presented here. The pressure at the inflow and outflow boundaries, respectively, is given by the relations

$$\begin{aligned} \mathscr{L}_{NR}^{-} p' = {} & \frac{\partial p'}{\partial t} - (1 - M) \frac{\partial p'}{\partial x} + (1 - M) \sum_m \sum_n \frac{\lambda_{mn}}{\beta} R_{mn}(r) \mathrm{e}^{\mathrm{i}m\theta} \\ & \int_0^t \left(\beta^2 \frac{\partial p_{mn}}{\partial x} - M \frac{\partial p_{mn}}{\partial t'} \right) J_1[(\lambda_{mn} \beta (t - t')] \, \mathrm{d}t' = \frac{2}{1 + M} \frac{\partial p_i'}{\partial t}, \end{aligned} \tag{2.12}$$

$$\begin{aligned} \mathscr{L}_{NR}^{+} p' = {} & \frac{\partial p'}{\partial t} + (1 + M) \frac{\partial p'}{\partial x} + (1 + M) \sum_m \sum_n \frac{\lambda_{mn}}{\beta} R_{mn}(r) \mathrm{e}^{\mathrm{i}m\theta} \\ & \int_0^t \left(\beta^2 \frac{\partial p_{mn}}{\partial x} - M \frac{\partial p_{mn}}{\partial t'} \right) J_1[(\lambda_{mn} \beta (t - t')] \, \mathrm{d}t' = 0, \end{aligned} \tag{2.13}$$

https://doi.org/10.1017/S0022112010000261 Published online by Cambridge University Press

where the subscript i on the right-hand side of (2.12) denotes the incident pressure wave. The axial velocity at the inflow boundary can be expressed in terms of the pressure via the relation,

$$p' + u_x = (1-M)\sum_m \sum_n \frac{\lambda_{mn}}{\beta} R_{mn}(r)\mathrm{e}^{\mathrm{i}m\theta} \int_0^t \{(u_{x_{mn}}(t') + Mp_{mn})J_1[\lambda_{mn}\beta(t-t')]\}\,\mathrm{d}t' + p_i' + u_{x_i}. \tag{2.14}$$

Note that the convolution integrals arise because the frequencies of the scattered waves are not generally known *a priori* because of nonlinear interactions. However, in the case where the unsteady fluctuations are assumed small throughout the domain, the problem is characterized only by the excitation frequency and the convolution integral simplifies to the known frequency domain boundary conditions (Atassi & Ali 2002; Atassi *et al.* 2004).

2.2. *Linear formulation: scattering from a compact heat source*

In this subsection, we derive the system of equations that arise in the compact heat source limit. We consider a small-amplitude acoustic mode in an annular duct, incident on a heat source whose axial extent is small relative to the acoustic wavelength. Assuming a monochromatic excitation characterized by the frequency, ω, the solution upstream of the heat source (region 1) consists of an incident and reflected acoustic wave and the pressure field solution (2.5) becomes:

$$p_1 = \sum_{n=1}^{n=\infty} a_{mn}^{+}\mathrm{e}^{\mathrm{i}m\theta}R_{mn}(r)\mathrm{e}^{\mathrm{i}(k_{mn_1}^{+}x-\omega t)} + a_{mn}^{-}\mathrm{e}^{\mathrm{i}m\theta}R_{mn}(r)\mathrm{e}^{\mathrm{i}(k_{mn_1}^{-}x-\omega t)}. \tag{2.15}$$

The region 1 velocity field is related to the pressure field by the linearized momentum equation. Downstream of the jump condition, the solution is a superposition of acoustic, vortical and entropic modes,

$$p_2' = \sum_{n=1}^{n=\infty}\sum_{m=-\infty}^{m=\infty} b_{mn}^{+}\mathrm{e}^{\mathrm{i}m\theta}R_{mn}(r)\mathrm{e}^{\mathrm{i}(k_{mn_2}^{+}x-\omega t)}, \tag{2.16}$$

$$\boldsymbol{u}_2 = \boldsymbol{u}_2^a + \sum_{n=1}^{n=\infty}\sum_{m=-\infty}^{m=\infty} \boldsymbol{C}_{mn}R_{mn}(r)\mathrm{e}^{\mathrm{i}(m\theta+\omega/U_2x-\omega t)}, \tag{2.17}$$

$$\rho_2' = \frac{p_2'}{{c_2}^2} + \sum_{n=1}^{n=\infty}\sum_{m=-\infty}^{m=\infty} F_{mn}R_{mn}(r)\mathrm{e}^{\mathrm{i}(m\theta+\omega/U_2x-\omega t)}. \tag{2.18}$$

Note that $\boldsymbol{u}_2^a$ denotes the velocity field induced by the acoustic wave and the second term in (2.17), $\boldsymbol{u}^g = \boldsymbol{u}_2 - \boldsymbol{u}_2^a$, is the convected, divergence-free velocity field induced by the vortical waves. The second term in (2.18) represents the convected density fluctuations induced by the entropy disturbances. The entropy perturbation, s', is related to the pressure and density through the equation of state and is expressed as

$$\frac{s'}{c_v} = \frac{p'}{P} - \frac{\gamma\rho'}{\overline{\rho}}. \tag{2.19}$$

The basis functions assumed for the vortical and entropic disturbances are the same as the acoustic modes since the scattered entropic and vortical disturbances can be expressed, using the Rankine–Hugoniot jump conditions, in terms of the acoustic velocity and density field at the jump condition. Note that due to the change in the

https://doi.org/10.1017/S0022112010000261 Published online by Cambridge University Press

speed of sound and Mach number, the axial wavenumber, k_{mn} changes across the jump. However, the acoustic eigenfunction, R_{mn}, depends only on the hub-tip ratio of the duct and the indices m and n. Since these do not vary in the upstream and downstream domains, this function remains the same.

The axial coefficient, $C_{x_{mn}}(r)$, is related to $C_{t_{mn}}(r)$ and $C_{r_{mn}}(r)$ by the divergence-free condition of the vortical velocity,

$$\nabla \cdot \boldsymbol{u}^g = 0. \tag{2.20}$$

Recall the radial velocity goes to zero when $r = r_h$ and $r = 1$ to satisfy the impermeability condition at the walls of the annular duct.

The Rankine–Hugoniot conditions can be derived from (2.1) in the limit where the control volume goes to zero. The resulting jump conditions are used to match the solutions upstream and downstream and determine the unknown coefficients of the acoustic, vortical and entropic waves. The jump conditions are expressed as

$$[\dot{m}] = [\rho \boldsymbol{v} \cdot \boldsymbol{n} A] = 0, \tag{2.21}$$

$$[pA + \dot{m}\boldsymbol{v}] = 0, \tag{2.22}$$

$$[\boldsymbol{v} \times \boldsymbol{n}] = 0, \tag{2.23}$$

$$[\dot{m}H] = \tilde{Q}, \tag{2.24}$$

where the brackets denote the change from region 1 to region 2, H is the total enthalpy and $\tilde{Q}$ is the integrated heat addition resulting from a concentrated heat source that can be decomposed into steady and unsteady terms $\tilde{Q} = Q + q'(t)$ where $|(q'(t))/Q| \ll 1$. A heat source or nozzle area change produces jumps in the mean flow field which are determined by substituting (2.4) into (2.21–2.24) and solving the leading-order jump conditions. To next order, we obtain the linearized jump conditions,

$$\left[\frac{\dot{m}'}{\bar{\dot{m}}}\right] = \left[\left(\frac{u_x}{U} + \frac{\rho'}{\bar{\rho}}\right)\right] = 0, \tag{2.25}$$

$$\left[\frac{p'}{\bar{\rho}U} + 2u_x + U\frac{\rho'}{\bar{\rho}}\right] = 0, \tag{2.26}$$

$$[u_\theta] = [u_r] = 0, \tag{2.27}$$

$$\left[H' + \frac{\dot{m}'}{\bar{\dot{m}}}\bar{H}\right] = \left[\frac{\gamma}{\gamma - 1}\left(\frac{P}{\bar{\rho}}\left(\frac{p'}{P} - \frac{\rho'}{\bar{\rho}}\right)\right) + Uu_x\right] + \frac{\dot{m}'}{\bar{\dot{m}}}\frac{Q}{\bar{\dot{m}}} = \frac{q'(t)}{\bar{\dot{m}}}, \tag{2.28}$$

where $[\bar{H}] = Q/\bar{\dot{m}}$. Equations (2.25)–(2.28) represent the unsteady conservation relations for mass, x-momentum, θ-momentum, r-momentum and energy, respectively. Using (2.27), the vortical wave amplitudes are related to the upstream and downstream acoustic wave amplitudes,

$$u_\theta^g = \left(u_{\theta_1}^a - u_{\theta_2}^a\right)|_{x=0}\, \mathrm{e}^{\mathrm{i}\omega/U_2(x-U_2t)}, \tag{2.29}$$

$$u_r^g = \left(u_{r_1}^a - u_{r_2}^a\right)|_{x=0}\, \mathrm{e}^{\mathrm{i}\omega/U_2(x-U_2t)}, \tag{2.30}$$

and the vortical waves convect downstream with the mean flow velocity, U_2. This relation also shows that the vortical waves depend on the incident, reflected and transmitted acoustic waves.

https://doi.org/10.1017/S0022112010000261 Published online by Cambridge University Press

The entropy can also be expressed in terms of the acoustic and vortical waves. The linearized entropy equation can be expressed as

$$\frac{\mathrm{D}_0 s'}{\mathrm{D}t} = -\frac{Q}{\overline{\rho}\overline{T}}\left(\frac{u'}{U} + \frac{p'}{P} - \frac{q'}{Q}\right), \tag{2.31}$$

where $\mathrm{D}_0/\mathrm{D}t \equiv \partial/\partial t + U(\partial/\partial x)$. Assuming time-harmonic disturbances $\{s', u', p', q'\} = \{\hat{s}, \hat{u}, \hat{p}, \hat{q}\}\mathrm{e}^{-\mathrm{i}\omega t}$ (2.31) can be expressed as

$$\frac{\partial}{\partial x}(\hat{s}\mathrm{e}^{-\mathrm{i}\omega/Ux}) = -\frac{Q\mathrm{e}^{-\mathrm{i}\omega/Ux}}{\overline{\rho}\overline{T}U}\left(\frac{\hat{u}}{U} + \frac{\hat{p}}{P} - \frac{\hat{q}}{Q}\right). \tag{2.32}$$

Assuming the heat source is a localized heat source at the origin of the domain, $Q = \bar{q}\delta(x)$, (2.32) can be integrated and the unsteady entropy due to mean heat source is

$$s'(\boldsymbol{x}, t) = \frac{-1}{\overline{\rho}_2\overline{T}_2U_2}\left[\bar{q}\left(\frac{\hat{u}_2}{U_2} + \frac{\hat{p}_2}{P_2}\right) - \hat{q}\right]_{x=0}\mathrm{e}^{\mathrm{i}\omega(x/U_2 - t)}. \tag{2.33}$$

This expression shows that the unsteady entropy is produced by both the mean heat source (through the pressure and velocity disturbances) and the unsteady heat source. Also, depending on the phase of the unsteady heat release the production of entropy can be either reinforced or suppressed.

The unsteady Rankine–Hugoniot conditions are then used to match the assumed form of the unsteady solutions at the interface between the upstream domain and the downstream domain. Substituting the unsteady solutions into (2.25) through (2.28) and using (2.29) and (2.30) yields a linear system of equations $\boldsymbol{Ax} = \boldsymbol{b}$ where the number of equations depends upon the number of Fourier–Bessel modes used to achieve an accurate match between the upstream and downstream solutions. The vector $\boldsymbol{b}$ contains the known incident wave which is fully specified by the circumferential mode order, m, the radial mode order, n, the hub-tip ratio and the reduced frequency, ω. In this work, the calculations are facilitated by MATLAB's GMRES routine which employs the generalized minimum residual method, from Saad & Martin (1986), to solve for each unknown modal coefficient.

In what follows, we analyse two problems using the compact source limit: (i) the scattering of acoustic waves in a constant area annular duct with heat addition and (ii) a converging nozzle without heat addition. Note that for the nozzle problem, the flow is isentropic and only four jump conditions are needed since the axial momentum and energy conditions reduce to the same condition. Nonlinear results are then computed that assess the ranges of validity of the compact source approximation by examining the impact of the heat source width and the incident wave amplitude on the scattered solution.

3. Results and discussion

3.1. *Plane wave scattering across a localized heat source*

In this section, we use the compact source formulation from § (2.2) to compute plane wave scattering due to a localized heat source. The heat source creates a jump in the mean flow which causes the incident acoustic wave to scatter into downstream travelling acoustic and entropic waves and an upstream travelling acoustic wave. The

https://doi.org/10.1017/S0022112010000261 Published online by Cambridge University Press

(Upstream conditions)	(Heat addition: downstream conditions)	Nozzle: downstream conditions
$M_1 = 0.300$	$M_2/M_1 = 1.806$	$M_2/M_1 = 1.806$
$P_1 = 0.714$	$P_2/P_1 = 0.798$	$P_2/P_1 = 0.872$
$\overline{\rho}_1 = 1.000$	$\overline{\rho}_2/\overline{\rho}_1 = 0.384$	$\overline{\rho}_2\overline{\rho}_1 = 0.907$
$c_1 = 1.000$	$c_2/c_1 = 1.441 \quad T_2/T_1 = 2.077$	$c_2/c_1 = 0.981 \quad T_2/T_1 = 0.962$
$A_1 = 1.000$	$A_2/A_1 = 1.000$	$A_2/A_1 = 0.623$

TABLE 1. Mean flow jump conditions for the cases with heat addition and area change.

results are compared with the transmission and reflection of acoustic waves in a compact nozzle.

When non-dimensionalized by the local steady pressure field, γP, the compact nozzle reflection and transmission coefficients can be determined solely from the Mach number upstream and downstream of the nozzle throat (Marble & Candel 1977). Motivated by this result, we compare the solutions for the adiabatic nozzle and the heated duct as a function of downstream Mach number with identical upstream flow conditions. Table 1 shows the mean flow jump for the compact nozzle and the heated duct where the area variation and heat addition have been chosen to yield the same Mach number ratio. Although the upstream mean flow and the downstream Mach number are the same, the mean flow pressure and density jumps are different. For example, the speed of sound decreases in the nozzle, $\bar{c}_2/\bar{c}_1 = 0.981$, and a large increase in the speed of sound and decrease in the density occur because of the heat addition, $\bar{c}_2/\bar{c}_1 = 1.441$ and $\bar{\rho}_2/\bar{\rho}_1 = 0.384$.

Figure 2 shows the non-dimensional reflection, transmission and entropy coefficients for the heated flow and nozzle subject to the same inlet conditions but different downstream Mach numbers. In the case of the nozzle, the downstream Mach number variation is achieved by varying the area ratio of the nozzle. In the case of the heated duct, the Mach number variation is achieved by varying a steady state heat source. Note the steady heat source limit, $q' = 0$, represents a canonical case where the reaction time is much longer than the acoustic forcing period (Dowling 1995). Figure 2(a) shows the transmitted wave coefficient versus downstream Mach number, M_2. In the heated duct, the transmission coefficient decreases faster than γP_2 with increasing Mach number, M_2, while the transmission coefficient for the nozzle increases slightly. Figure 2(b) shows a comparison of the reflected wave amplitude versus downstream Mach number for both cases. As the mean flow jump increases, larger reflections result in both cases. The nozzle exhibits larger reflections than the heated duct for the same Mach number ratio. However, the heated duct produces entropy waves because of the heat addition which convect downstream. The entropy wave amplitude, shown in figure 2(c), increases significantly with the increasing downstream Mach number jumps for the heated duct. Thus, it is evident that some of the acoustic energy of the incident acoustic wave is scattered into entropic disturbances.

To better understand the transfer of energy in the nozzle and heated duct problems, we examine the acoustic power. The acoustic power associated with the incident acoustic wave, E_{in}, and the acoustic power leaving the computational domain, E_{out}, are defined as,

$$E_{in} = \int_{\partial\Omega} [I_{inc}] \cdot \hat{n} \, \mathrm{d}A \tag{3.1}$$

https://doi.org/10.1017/S0022112010000261 Published online by Cambridge University Press

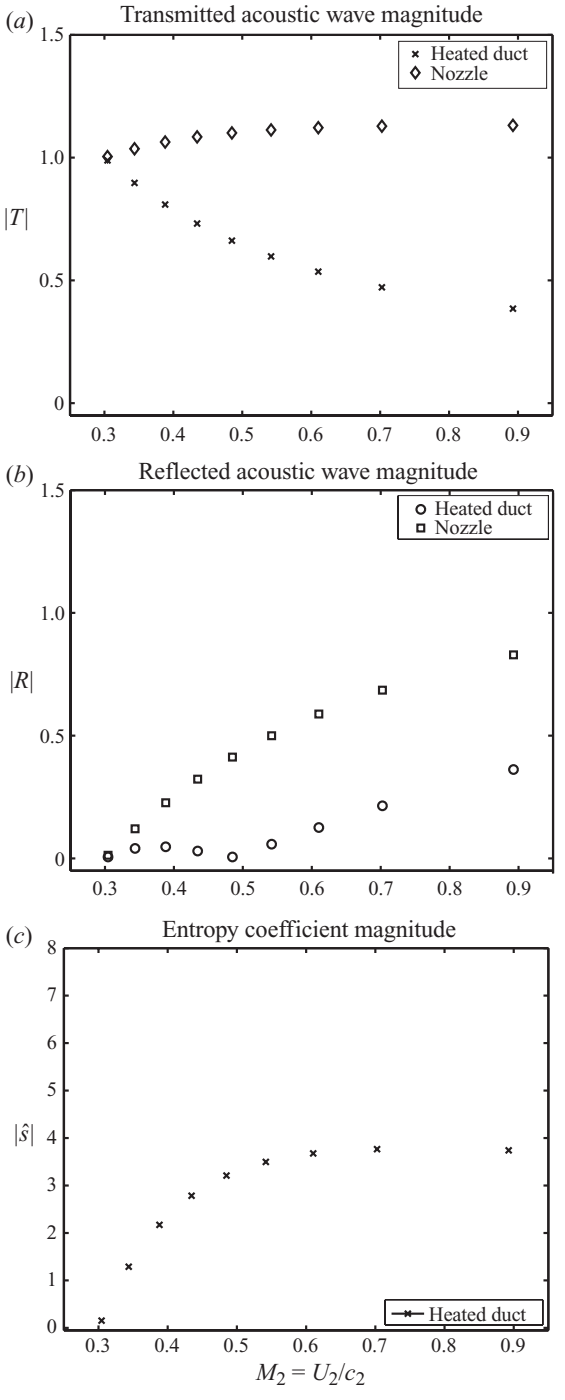


FIGURE 2. Scattered wave magnitudes for heated duct versus nozzle with incident plane wave (m = 0). Upstream Mach number $= U_1/c_1 = 0.3$. (*a*) Transmitted acoustic wave magnitude, $|T| = |b^+/a^+|/(\gamma P_2)$, (*b*) reflected acoustic wave magnitude, $|R| = |a^-|/|a^+|$ and (*c*) entropy wave magnitude, $|\hat{s}| = |s'|/c_v$, versus downstream Mach number, U_2/c_2.

https://doi.org/10.1017/S0022112010000261 Published online by Cambridge University Press

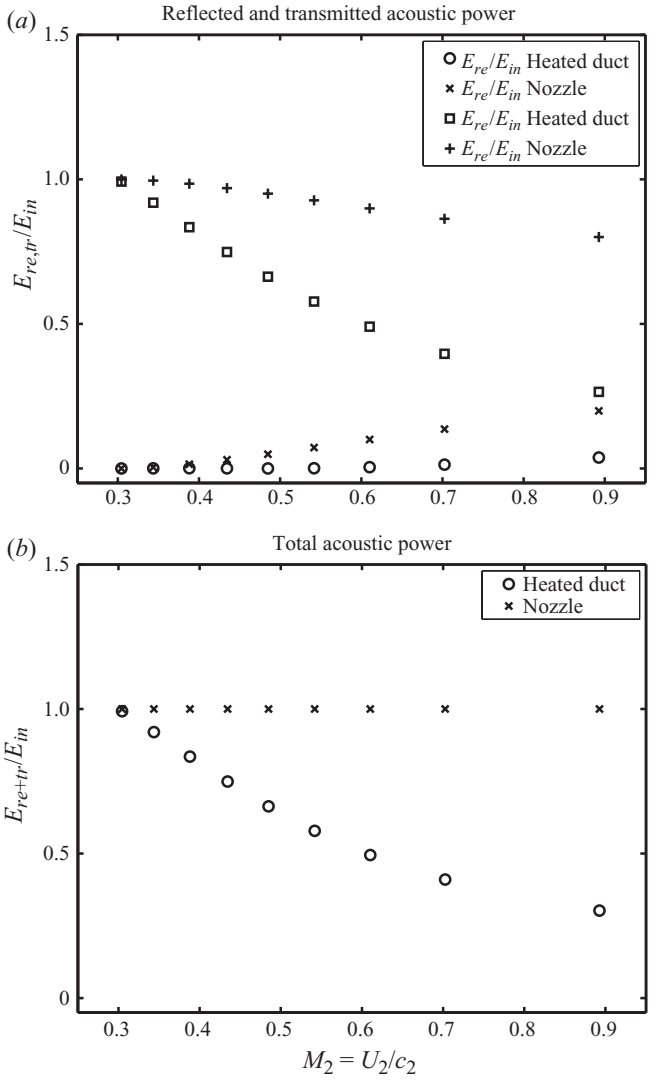


FIGURE 3. Sound power for heated duct versus nozzle with incident plane wave (m = 0). Upstream Mach number $= U_1/c_1 = 0.3$. (*a*) Transmitted and reflected acoustic wave sound power versus downstream Mach number, U_2/c_2 and (*b*) sum of transmitted and reflected acoustic wave sound power.

and

$$E_{out} = \int_{\partial\Omega} [I_{re} + I_{tr}] \cdot \hat{n} \, \mathrm{d}A, \tag{3.2}$$

where I is given by,

$$I = \left(\frac{p'}{\overline{\rho}} + \boldsymbol{u} \cdot \boldsymbol{U} \right) (\overline{\rho}\boldsymbol{u} + \rho' \boldsymbol{U}). \tag{3.3}$$

The acoustic power of the incident, reflected and the transmitted waves for the respective duct with heat addition and isentropic nozzle is shown in figure 3. In each case, the power has been normalized by that of the incident acoustic wave.

https://doi.org/10.1017/S0022112010000261 Published online by Cambridge University Press

Figure 3(a) shows that the reflected and transmitted acoustic energy of the heated duct is significantly lower than the nozzle case suggesting that a significant portion of the incident acoustic energy has scattered into entropic disturbances. Figure 3(b) shows the outgoing acoustic energy, $E_{re} + E_{tr}$. In the nozzle problem $E_{in} = E_{out}$, while for the heated duct $E_{in} > E_{out}$. For the heated duct, the outgoing acoustic energy decreases rapidly with downstream Mach number, until about $M_2 = 0.5$ where the rate of reduction in energy is less steep. This is also the Mach number where the rate of increase in the entropic amplitude starts to decrease.

Equation (2.33) shows that unsteady heat release may act to increase or suppress the entropy waves convecting downstream. To further understand the role of the scattered entropy waves on the scattered acoustic waves, we consider a second canonical case of unsteady heat addition where the rate of heat input is proportional to fluctuations in the mass flow rate, $q'/\bar{q} = \dot{m}'/\bar{\dot{m}}$ (Dowling 1995). In this case, the production of entropy is suppressed by the heat addition. Figure 4 shows the scattered wave coefficients for the two canonical heat duct cases and the adiabatic nozzle. Figure 4(c) shows that very little entropy is produced when the unsteady heat source is proportional to fluctuations in the mass flow rate, and as a result, the reflected and transmitted acoustic wave coefficients, shown in figure (4a,b), increase relative to the $q' = 0$ limit. Moreover, this unsteady heat addition case shows scattered solutions which are very similar to the nozzle. The trends for the steady and unsteady heat addition cases suggest that it is the production of entropy which differentiates the acoustic scattering in the heated duct from the adiabatic nozzle problem.

3.2. *Circumferential mode scattering by a localized mean heat source*

The plane wave scattering, analysed in the previous section, depends on the mean flow jump and is independent of the frequency of the incident wave. In this section, we investigate the scattering of an incident circumferential acoustic mode into acoustic, entropic and vortical disturbances. In particular, we study the effect of the mean flow jump, the frequency of the excitation and the circumferential mode number, m, on the scattering of the incident wave.

3.2.1. *Effect of heat addition and reduced frequency on circumferential mode scattering*

Figure 5 shows the acoustic, vortical and entropic wave amplitudes with $m = 1$ over a range of downstream Mach numbers. Each Mach number corresponds to different quantities of heat addition and the same imposed upstream conditions which are provided in table 1. The reduced frequency at the inlet is $\omega = 4\pi/3$. As the Mach number jump increases, the amplitudes of the entropy wave and the reflected acoustic wave increase while the transmitted acoustic wave decreases. Vorticity waves are also produced but their amplitudes are relatively low compared to the entropy waves. Note that the trends for the acoustic and entropic wave amplitudes with an incident circumferential mode are similar to that of the plane wave.

Figure 6 shows the scattered field amplitudes versus incident wave frequency. In this case, the upstream and downstream Mach numbers are fixed: $M_1 = 0.3$ and $M_2 = 0.61$. As a reference, the cutoff ratio, $\omega/(\lambda_{mn}\beta)$, is plotted alongside the coefficient magnitudes. For propagating modes which approach cutoff, there is a large rise in the transmitted and reflected acoustic waves. The vortical waves also increase but the entropy wave amplitude significantly decreases. As the frequency increases and the cutoff ratio approaches 2.0, the vortical and acoustic wave amplitudes decrease and the entropy wave amplitude increases. Beyond a cutoff ratio of 2.0 the results

https://doi.org/10.1017/S0022112010000261 Published online by Cambridge University Press

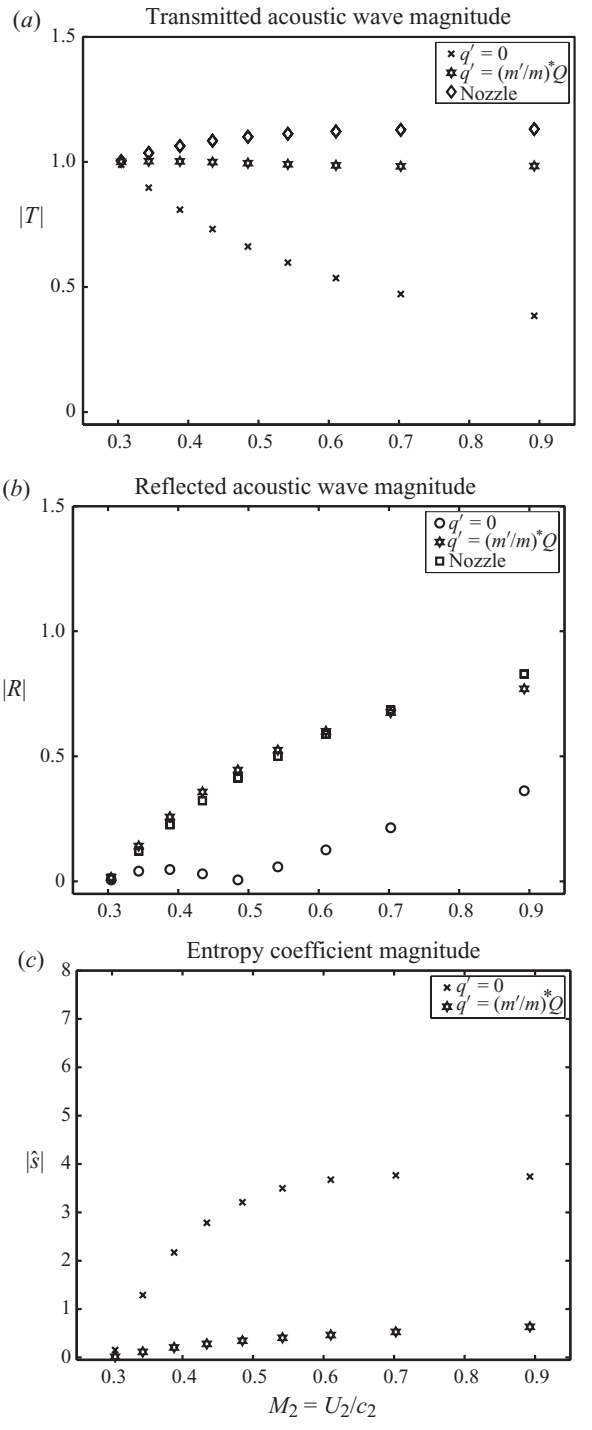


FIGURE 4. Scattered wave magnitudes for heated duct, $q' = 0$ and $q' = (m'/\bar{m})(Q)$, versus nozzle with incident plane wave (m = 0). Upstream Mach number $= U_1/c_1 = 0.3$. (*a*) Transmitted acoustic wave magnitude, $|T| = |b^+/a^+|/(\gamma P_2)$, (*b*) reflected acoustic wave magnitude, $|R| = |a^-|/|a^+|$ and (*c*) entropy wave magnitude, $|\hat{s}| = |s'|/c_v$, versus downstream Mach number, U_2/c_2.

https://doi.org/10.1017/S0022112010000261 Published online by Cambridge University Press

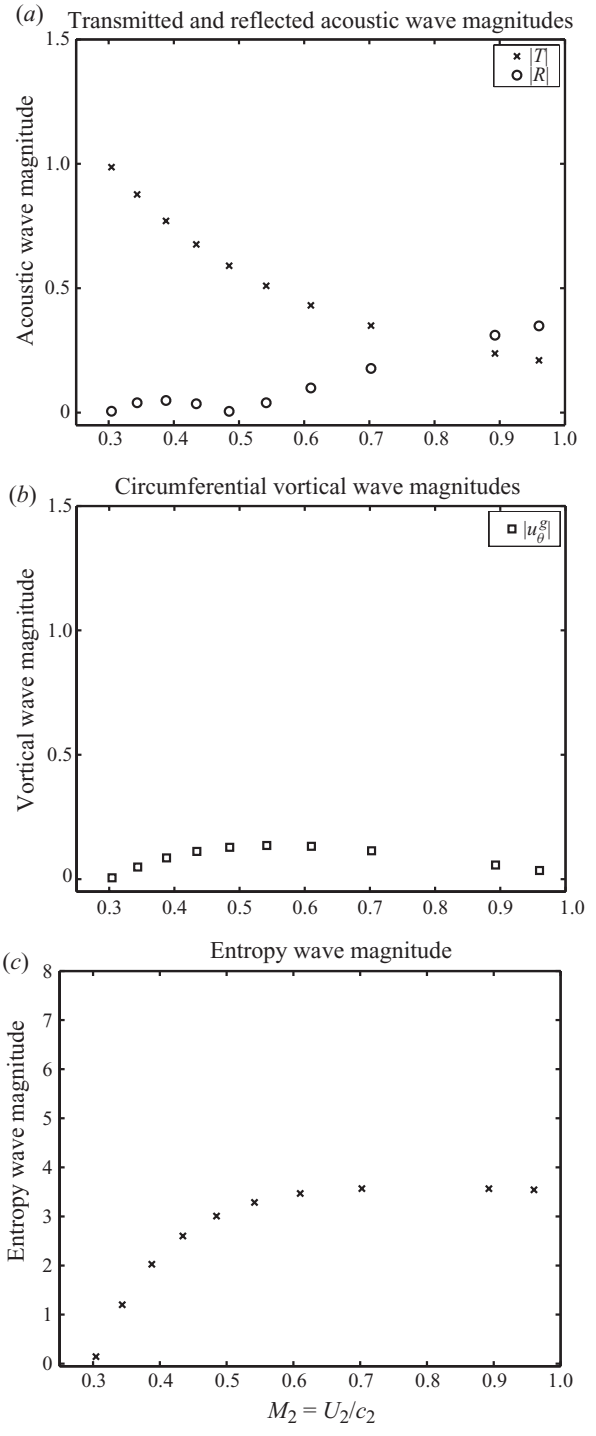


FIGURE 5. Magnitude of scattered waves for heated duct with incident circumferential wave ($m = 1$). Note that $\omega = 4\pi/3$. Upstream Mach number $= U_1/c_1 = 0.3$. (a) Transmitted and reflected acoustic wave magnitudes, $|T| = |b^+|/|a^+|$, $|R| = |a^-|/|a^+|$, (b) circumferential vortical wave magnitude, $|u_\theta^g| = |C_t|/|a^+|$ and (c) entropy wave magnitude, $|\hat{s}| = |s^{'}|/c_v$.

https://doi.org/10.1017/S0022112010000261 Published online by Cambridge University Press

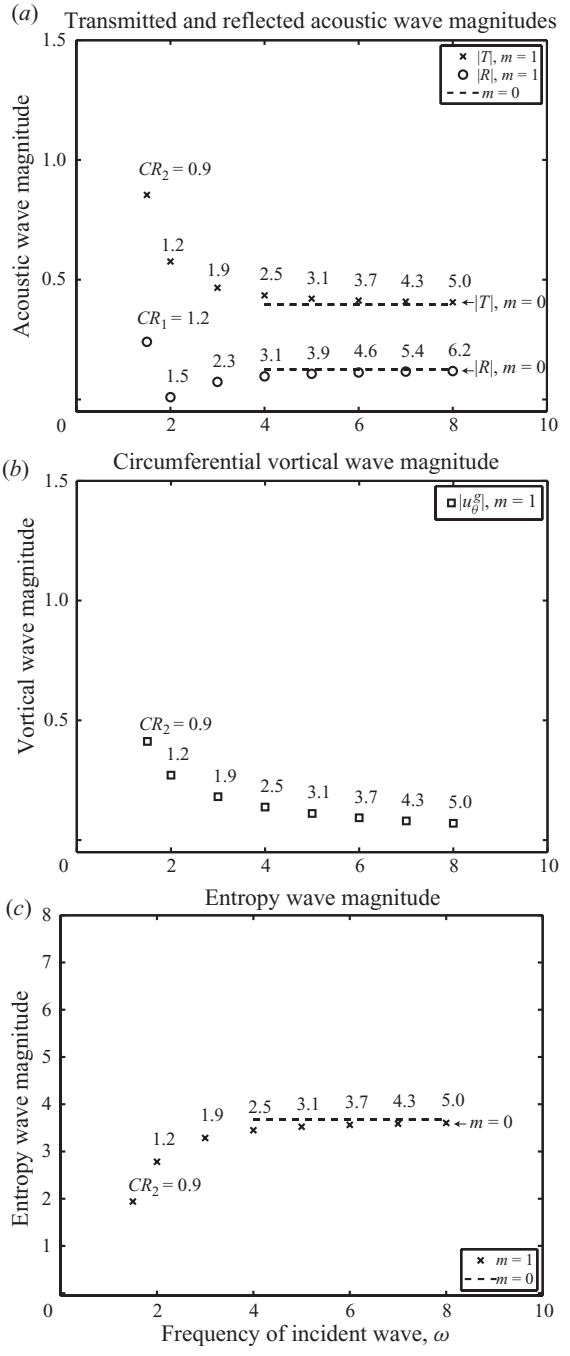


FIGURE 6. Magnitude of scattered amplitudes versus frequency of incident circumferential wave. Comparison to incident plane wave. Upstream Mach number $= U_1/c_1 = 0.3$. Downstream Mach number $= U_2/c_2 = 0.61$. Cutoff ratios plotted above symbols. (*a*) Transmitted and reflected acoustic wave magnitudes, $|T| = |b^+|/|a^+|$, $|R| = |a^-|/|a^+|$, (*b*) circumferential vortical wave magnitude, $|u_\theta^g| = |C_t|/|a^+|$ and (*c*) entropy wave magnitude, $|\hat{s}| = |s'|/c_v$.

https://doi.org/10.1017/S0022112010000261 Published online by Cambridge University Press

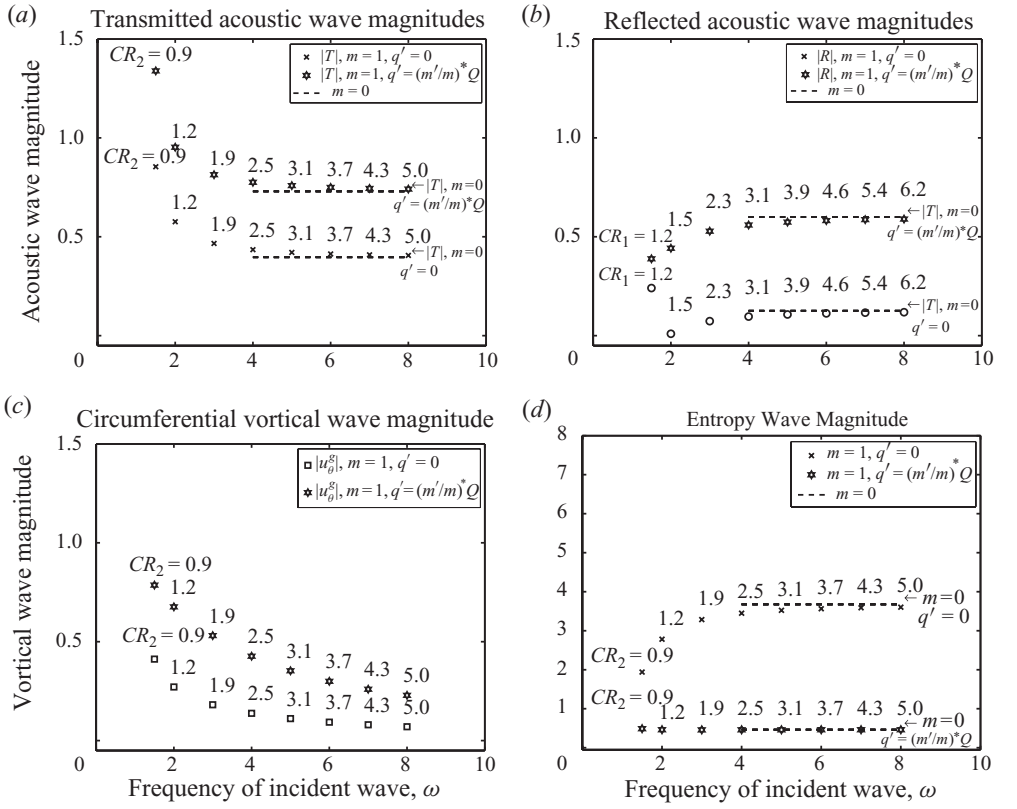


FIGURE 7. Magnitude of scattered amplitudes versus frequency of incident circumferential wave. Steady and unsteady heat addition in comparison to incident plane wave. Upstream Mach number $= U_1/c_1 = 0.3$. Downstream Mach number $= U_2/c_2 = 0.61$. Cutoff ratios plotted above symbols. (*a*) Transmitted acoustic wave magnitudes, $|T| = |b^+|/|a^+|$, (*b*) reflected acoustic wave magnitudes, $|R| = |a^-|/|a^+|$, (*c*) circumferential vortical wave magnitude, $|u_\theta^g| = |C_t|/|a^+|$ and (*d*) entropy wave magnitude, $|\hat{s}| = |s'|/c_v$.

appear to asymptote towards the plane wave results. There is also clear delineation in amplitudes for the calculations where the incident acoustic wave is cutoff.

This behaviour is not unexpected from the inspection of (2.29), (2.30) and (2.33). Equation (2.33) shows that the entropy depends on the downstream perturbation pressure and velocity, both of which decrease rapidly at cutoff. The vortical wave behaviour, however, is quite different. Equation (2.29) shows that the vortical waves depend upon the circumferential velocity component induced by the acoustic waves. Furthermore, since the basis functions of both the upstream and downstream acoustic waves follow that of the upstream incident wave, we may use (2.11) to understand that near cutoff, the circumferential acoustic velocity is large compared to the axial velocity. Specifically, the ratio of circumferential acoustic velocity to axial acoustic velocity is governed by m/k_{mn}, which increases with decreasing cutoff ratio. Thus, near cutoff, the scattered vortical wave coefficients are expected to increase relative to the scattered entropic wave which depends on the axial velocity component.

To understand the role of unsteady heat release on the circumferential acoustic modes, we consider the effect of unsteady heat addition where $q'/\bar{q} = \dot{m}'/\bar{\dot{m}}$. Figure 7 shows the scattered wave solutions with and without unsteady heat release. Note that

https://doi.org/10.1017/S0022112010000261 Published online by Cambridge University Press

$M_2 = 0.39$	$CR_1 = 1.215$	$m/k_{11}^{+} = 2.16$	$\omega_1 = 2.1$	$m = 1$
	$CR_1 = 1.215$	$m/k_{11}^{+} = 2.19$	$\omega_1 = 4.1$	$m = 2$
	$CR_1 = 1.215$	$m/k_{11}^{+} = 2.22$	$\omega_1 = 6.1$	$m = 3$
$M_2 = 0.39$	$CR_1 = 2.321$	$m/k_{11}^{+} = 0.503$	$\omega_1 = 4.0$	$m = 1$
	$CR_1 = 2.346$	$m/k_{11}^{+} = 0.502$	$\omega_1 = 8.0$	$m = 2$
	$CR_1 = 2.331$	$m/k_{11}^{+} = 0.514$	$\omega_1 = 11.7$	$m = 3$

TABLE 2. Acoustic parameters used in the constant cutoff ratio study with a mean heat source resulting in $M_2/M_1 = 0.39/0.3$. The first column contains the downstream Mach number. The second through fourth columns show the cutoff ratio, circumferential mode to axial wavenumber ratio, reduced frequency and circumferential mode number utilized to maintain the cutoff ratios constant for the incident acoustic mode.

the choice of unsteady heat release acts to suppress the production of entropy and more energy is scattered into the acoustic solutions. However, at cutoff ratios close to unity, the amplitude of the scattered vortical waves is larger providing another means to transfer energy from the outgoing acoustic waves.

3.2.2. *Circumferential mode scattering sensitivity to cutoff ratio*

The results in § 3.2.1 suggest that the cutoff ratio is an important parameter in determining the scattering of the incident waves across the interface. Inspection of (2.11) shows that the velocity field produced by the incident pressure wave depends on the Mach number, the cutoff ratio and m/k_{mn}. Moreover, (2.29) shows that the circumferential vortical velocity depends on the acoustic velocity jump. In this section, we examine whether the scattered amplitudes, at a given Mach number, can be expressed solely in terms of the cutoff ratio parameter, $\omega/(\lambda_{mn}\beta)$, instead of both the frequency and circumferential mode number, m.

We consider three different heat sources producing different downstream Mach numbers for the same upstream conditions given in table 1. We then impose incident wave excitations with different frequencies and circumferential mode order but the same cutoff ratio. Constant cutoff ratios are obtained by selecting a circumferential mode order, m, and varying the frequency until the desired cutoff ratio is obtained. A summary of the parameters used to achieve a nearly constant cutoff ratio for one of the heat sources is presented in table 2. The first three columns of table 2 show the parameters that determine the induced axial and circumferential acoustic velocity components. The last two columns show the frequencies and spinning mode orders utilized to achieve a nearly constant cutoff ratio for the incident acoustic mode. Note that, in the cases considered, the parameter, m/k_{mn}, which affects the circumferential velocity is also nearly constant.

Figures 8(a) and 8(b) show the transmitted and reflected acoustic wave coefficients versus Mach number, M_2, for various incident waves with the same cutoff ratios. For the first radial mode, cutoff ratios of 1.0–2.0 were targeted for the waves in the downstream domain. The scattered acoustic waves produced upstream and downstream of the heat source are nearly identical when the cutoff ratio is the same. Additionally, figures 9 and 10 show the θ-vortical, x-vortical and entropy wave magnitudes. The θ-vortical, x-vortical and entropy wave magnitudes also collapse with the cutoff ratio. Since the cutoff ratio is a function of radial mode order, it is only possible to hold the cutoff ratio for one radial mode at a time. The present results showing nearly identical results at the same cutoff ratio imply that little of

https://doi.org/10.1017/S0022112010000261 Published online by Cambridge University Press

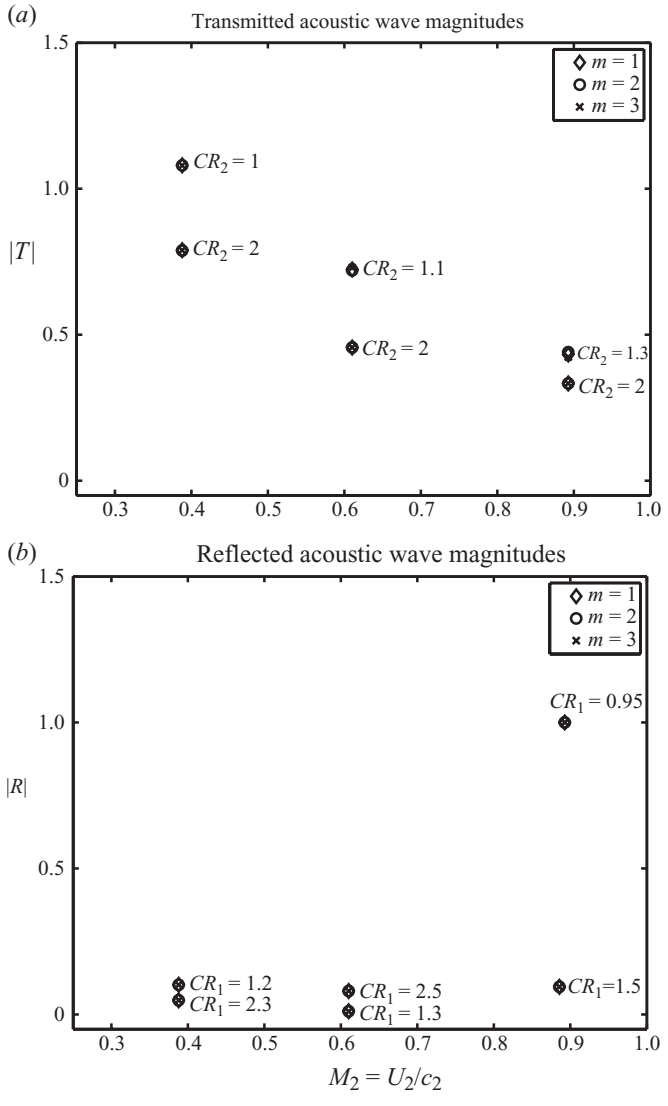


FIGURE 8. Cutoff ratio collapse. Magnitude of scattered acoustic waves for different incident circumferential mode orders. Upstream Mach number $= U_1/c_1 = 0.3$. (a) Transmitted acoustic wave magnitude, $|T| = |b^+|/|a^+|$, (b) reflected acoustic wave magnitude, $|R| = |a^-|/|a^+|$, versus downstream Mach number, U_2/c_2.

the incident acoustic wave scatters into higher-order radial modes. This is indeed the situation, since the flow field and geometry considered exhibit no radial variation across the annulus.

3.3. *Euler results: effect of finite source thickness on acoustic scattering*

In the previous sections, the scattering from a jump condition produced by a discrete heat source jump condition was considered. The equations for the compact source limit, where the heat source is represented by jump conditions, are normal both upstream and downstream of the jump. In this case, the coupling between the acoustic, vortical and entropic waves occurs only through the jump conditions and the

https://doi.org/10.1017/S0022112010000261 Published online by Cambridge University Press

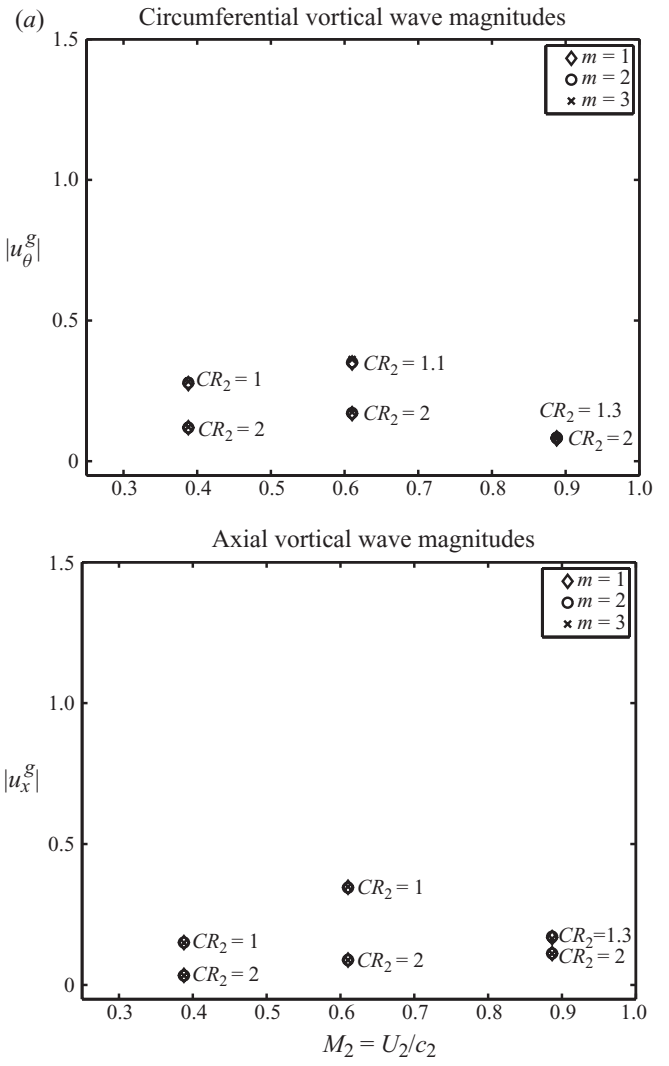


FIGURE 9. Cutoff ratio collapse. Upstream Mach number $= U_1/c_1 = 0.3$. (*a*) Magnitude of scattered circumferential vortical wave, $|u_\theta^g| = |C_t|/|a^+|$ and (*b*) Magnitude of scattered x-vortical wave, $|u_x^g|$, versus downstream Mach number, U_2/c_2, for different incident circumferential mode orders.

eigenfunction solutions upstream and downstream of the jump are orthogonal. When the heat source has finite thickness, the mean flow is non-uniform and the linearized operator of the system of equations is locally non-normal. Coupling between the acoustic, vortical and entropic modes may occur (Chagelishvili *et al.* 1997; Golubev & Atassi 1998; Atassi 2003; Atassi 2007; George & Sujith 2009), but it is confined to the local region of non-uniform flow.

In this section, the effect of the width of the heat source is studied by solving the Euler equations subject to an incident acoustic wave where the amplitude of the heat source is adjusted, depending on the width of the heat source, to maintain constant flow conditions upstream and downstream of the heat source. We assume a Gaussian heat source characterized by the amplitude, A, and width,

https://doi.org/10.1017/S0022112010000261 Published online by Cambridge University Press

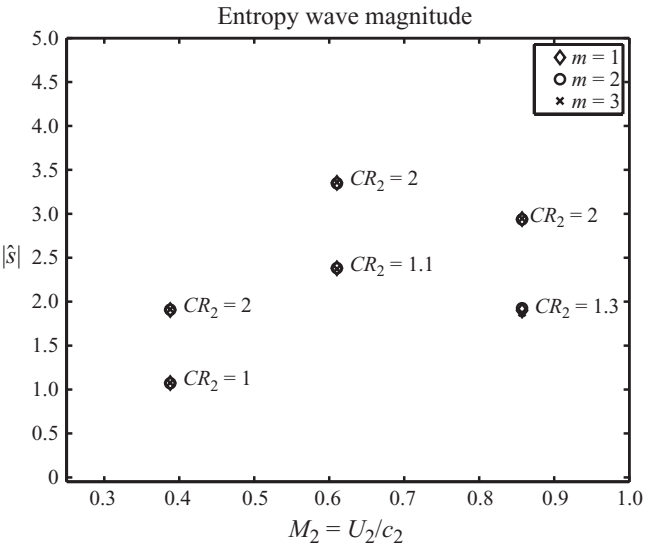


FIGURE 10. Cutoff ratio collapse. Upstream Mach number $= U_1/c_1 = 0.3$. (*a*) Magnitude of scattered entropy wave, $|\hat{s}| = |s'|/c_v$, versus downstream Mach number, U_2/c_2, for different incident circumferential mode orders.

σ, where $Q(x) = A\exp(-x^2/\sigma^2)$. To isolate the effect of the heat source width on the scattered solution, the amplitude of the incident acoustic wave is small, $a_i = 0.001$.

3.3.1. *Scattering by a finite thickness heat source*

An incident acoustic wave with a mean flow characterized by heat sources of different widths and amplitudes is considered. Three heat sources adding different levels of heat are studied. For each of the three cases, four different heat source widths producing the same net heat addition are analysed. Figure 11 shows the Gaussian heat source distributions of different widths for the case with moderate heat energy which is characterized by the Mach number rise, $M_2 = 0.70$. Note that as the width of the heat source increases, the peak amplitude decreases to sustain the same net heat addition. The imposed upstream Mach number in each case is $M_1 = 0.48$. The downstream Mach numbers for the three cases considered are: $M_2 = 0.56$, 0.70 and 0.89.

Figure 12 shows the reflected and transmitted acoustic waves for all three downstream Mach numbers, M_2. For each of the cases, several different heat source widths, $\sigma = 0.05, 0.1, 0.2, 0.4$, are considered. As the width increases, the results start to deviate from the compact source limit. In each case, the trend shows the transmitted wave amplitudes increasing and the reflected wave amplitude decreasing as the axial extent of the heat source broadens. The variation in scattered wave amplitude is more visible in the shorter wavelength reflected waves than the downstream-going scattered wave. The scattered wave sensitivity to the width of the heat source is most visible in the upstream-going scattered wave associated with the largest heat addition case corresponding to a downstream Mach number, $M_2 = 0.89$. Here the upstream scattered acoustic wave amplitudes are noticeably smaller than the compact source limit.

https://doi.org/10.1017/S0022112010000261 Published online by Cambridge University Press

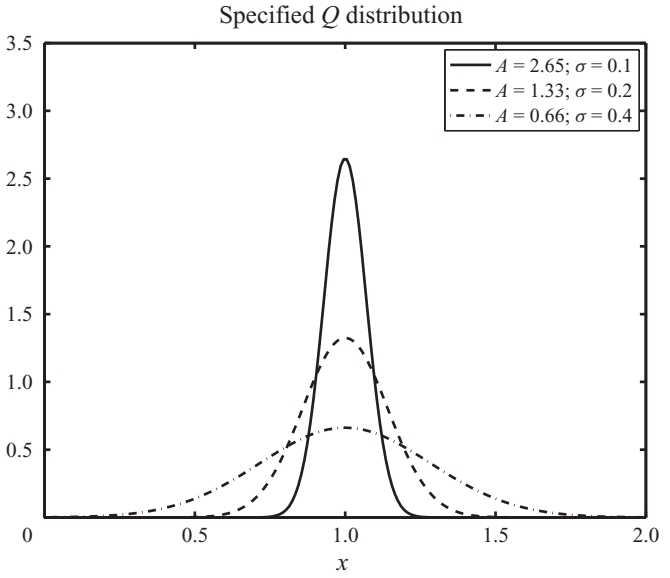


FIGURE 11. Heat source distributions with different widths, but constant energy.

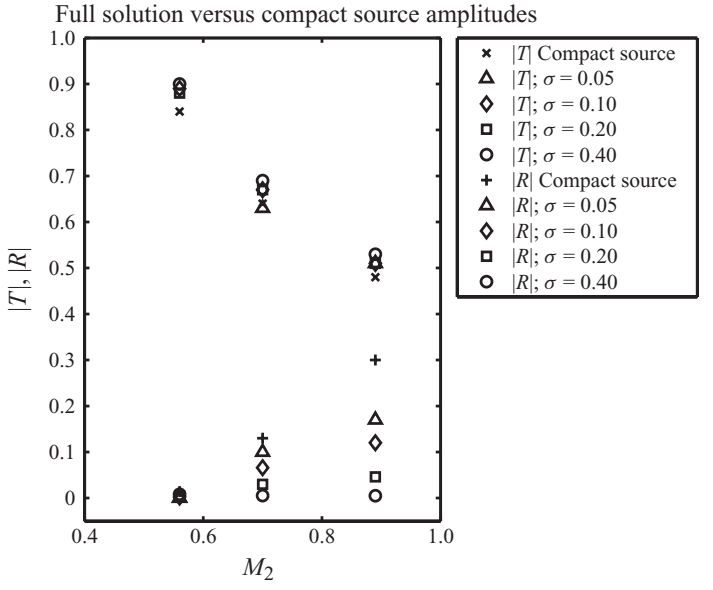


FIGURE 12. Incident plane wave: acoustic amplitudes for heat source distributions with different widths, but constant energy. Three different downstream Mach numbers, $M_2 = 0.56$, 0.70, and 0.89.

Figure 13 shows an overlay of the various solutions for the case with a downstream Mach number equal to 0.70. Figure 13(*a–c*) shows the axial pressure, entropy and velocity distributions for four different heat source widths ranging from zero thickness, the compact source limit, to the width resulting from $\sigma = 0.4$. The pressure, entropy, and x-velocity solutions are plotted as a function of axial coordinate. The Euler solutions show a smooth transition across the heat source while the compact source

https://doi.org/10.1017/S0022112010000261 Published online by Cambridge University Press

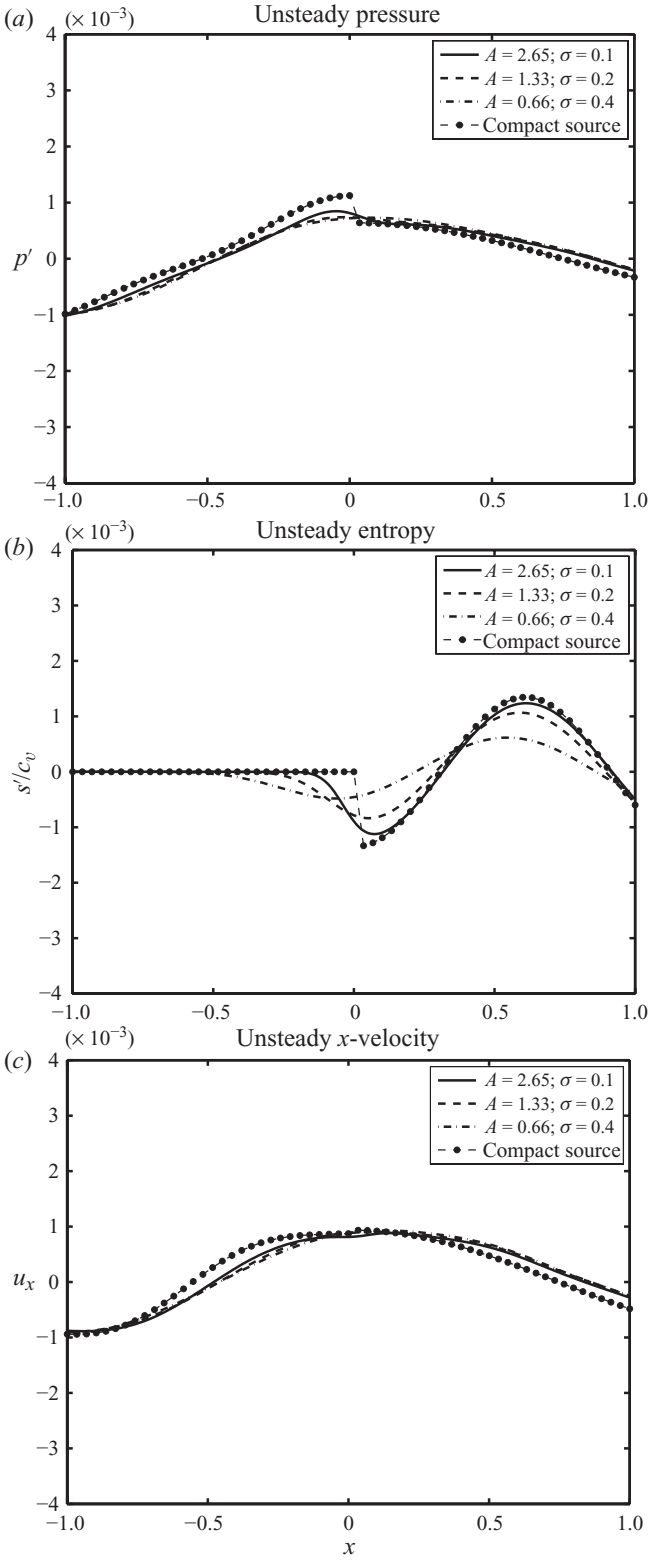


FIGURE 13. Mid-Q case, $M_2 = 0.70$. Effect of heat source width on unsteady parameters (*a*) Pressure, (*b*) entropy (*c*) x-velocity. Incident plane wave.

https://doi.org/10.1017/S0022112010000261 Published online by Cambridge University Press

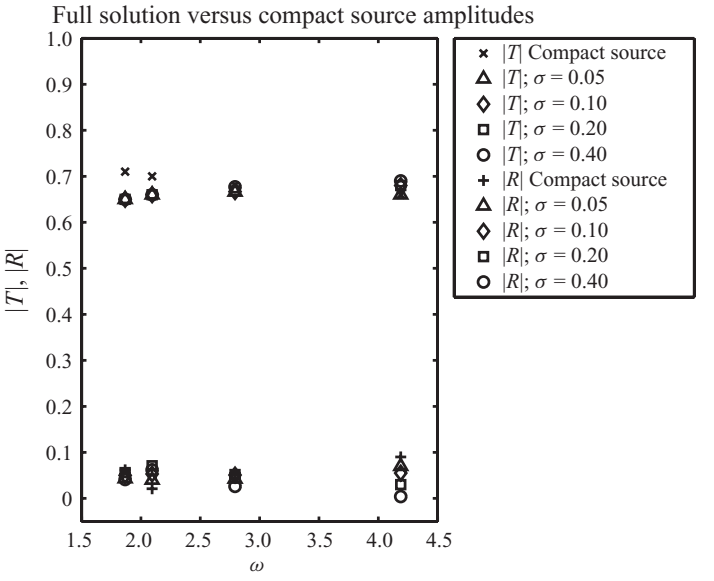


FIGURE 14. Incident $m = 1$ wave: acoustic amplitudes versus frequency for heat source distribution with jump $M_1 = 0.3$, $M_2 = 0.70$ and different frequencies: $\omega = 1.87$, $2\pi/3$, $8\pi/9$ and $4\pi/3$.

exhibits a jump in the pressure and entropy solutions. Despite the local variation, the solutions upstream and downstream match the compact limit solution quite well. The largest variations between the solutions are visible in the entropy which decreases in amplitude as the width of the heat source increases. As the amplitude of the entropy wave decreases, the amplitude of the downstream-going scattered acoustic wave increases slightly. This general trend of decreasing entropy with increasing width is observed in the three mean flow jumps considered. Figure 13 also shows that the full solution approaches the compact source in the limit of narrower heat source distributions and suggests the class of problems for which the compact source approximation may be used.

The scattering of a circumferential wave, $m = 1$, is also presented for several heat source thicknesses. A single mean flow jump is considered, $M_2 = 0.70$, with four different frequencies: $\omega = 4\pi/3$, $8\pi/9$, $2\pi/3$ and 1.87. Figure 14 shows the transmitted and reflected acoustic amplitudes versus incident wave frequency, ω. Like the plane wave, the narrowest heat source width approaches the solution of the compact source model for all of the frequencies. The sensitivity of the solutions to the width of the heat source is more visible for the higher frequencies where the wavelength of the upstream and downstream acoustic waves is of similar order to the thickness of the heat source.

3.4. *Nonlinear scattering: effect of incident wave amplitude on outgoing acoustic waves*

In this section, we solve the Euler equations and vary the amplitude of the incident wave to examine how nonlinear effects modify the solution. Figure 15 shows line plots of the pressure for two incident waves with amplitudes, $a_i = 0.01, 0.05$. To aid the comparison between the small and moderate amplitude solutions, the small amplitude solution with $a_i = 0.01$ has been scaled by a factor of five. Comparison of the line

https://doi.org/10.1017/S0022112010000261 Published online by Cambridge University Press

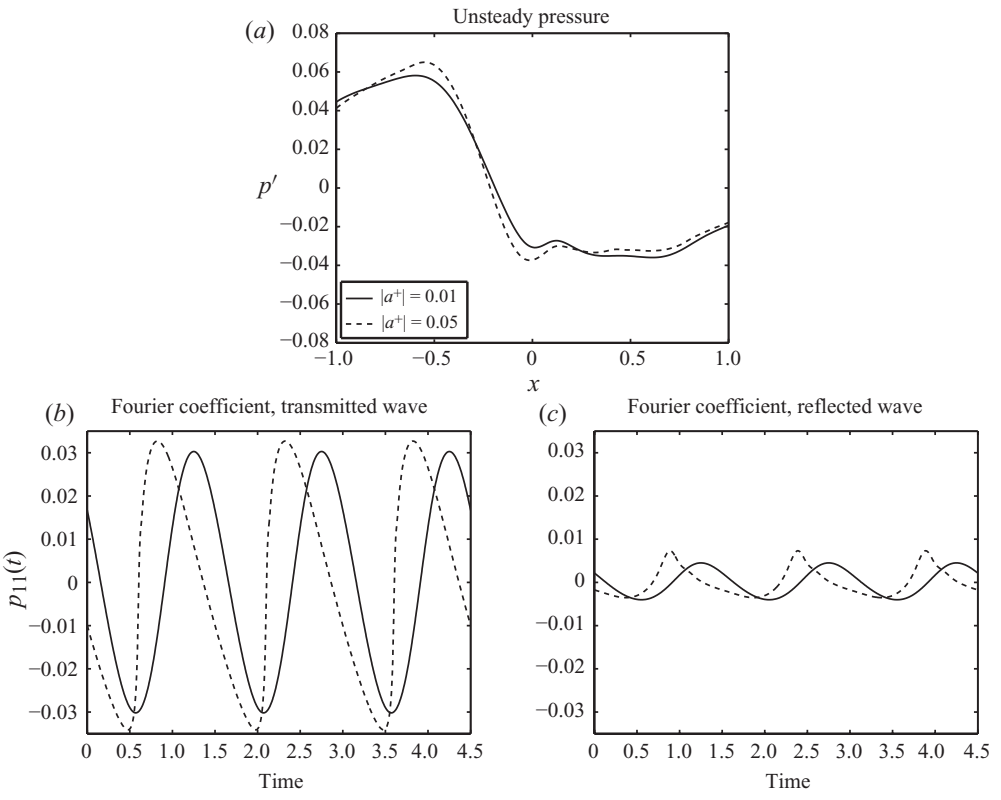


FIGURE 15. Effect of incident wave amplitudes, 0.01 and 0.05. (*a*) unsteady pressure solution, (*b*) Fourier coefficient of transmitted wave, (*c*) Fourier coefficient of reflected wave.

plots near the location of the heat source shows a steepening in the pressure wave fronts.

To examine the effect of the amplitude on the time evolution, figure 15(*b*,*c*) shows the time history of the last three periods of the converged scattered wave solutions at the inlet and the exit of the domain. The small amplitude solution has been scaled by a factor of five for plotting purposes and shows a sinusoidal behaviour in time which is characterized by the dominant excitation frequency, ω. The scattered acoustic waves at the inlet and exit for the larger amplitude disturbance are slightly higher in amplitude. Moreover, they exhibit a different oscillatory behaviour because of the production of higher harmonic frequencies which alter both the amplitude and sinusoidal character of the oscillations.

4. Conclusions

The range of validity of the compact source limit and the effect of circumferential mode excitations on the scattering of acoustic waves into vortical, entropic and reflected and transmitted acoustic waves are studied. The scattering of circumferential waves is characterized by the mean flow Mach number, reduced frequency and circumferential mode order of the imposed incident wave. For the cases considered in this paper where little scattering into radial modes occurs, it is found that the solutions can be characterized by a single parameter: the cutoff ratio, $\omega/(\beta\lambda_{mn})$. Incident waves with large cutoff ratios approach the results for plane wave excitations. However, for

https://doi.org/10.1017/S0022112010000261 Published online by Cambridge University Press

cutoff ratios closer to unity, significant deviations from the plane wave results occur. When the axial extent of the heat source is on the order of the acoustic wavelength, the scattered solution is also modified. In this case, the entropy wave amplitude is diminished and the downstream scattered acoustic wave amplitude is enhanced.

Understanding the basic interactions of acoustic waves in heated flows is an important first step in understanding how energy is transferred in these applications. Moreover, mean flow quantities and their gradients are much easier to measure than unsteady fluctuations in heat release. Thus, the effectiveness and limitations of models describing the interaction of acoustic waves in heated flows may be easier to realize than complex simulations trying to capture all of the physics and unsteady interactions occurring in combusting flows.

REFERENCES

Atassi, H. M., Ali, A. A., Atassi, O. V. & Vinogradov, I. V. 2004 Scattering of incident disturbances by an annular cascade in a swirling flow. *J. Fluid Mech.* **499**, 111–138.

Atassi, O. V. 2003 Computing the sound power in non-uniform flow. *J. Sound Vib.* **266**, 75–92.

Atassi, O. V. 2007 Propagation and stability of the vorticity-entropy waves in a non-uniform flow. *J. Fluid Mech.* **545**, 149–176.

Atassi, O. V. & Ali, A. 2002 Inflow/outflow conditions for internal time-harmonic Euler equations. *J. Comput. Acoust.* **10**, 155–182.

Atassi, O. V. & Galan, J. M. 2008 The implementation of nonreflecting boundary conditions for the nonlinear Euler equations. *J. Comput. Phys.* **227**, 1643–1662.

Bohn, M. S. 1977 Response of a subsonic nozzle to acoustic and entropy disturbances. *J. Sound Vib.* **52**, 283.

Chagelishvili, G. D., Tevzadze, A. G., Bodo, G. & Moiseev, S. S. 1997 Linear mechanism of wave emergence from vortices in smooth shear flows. *Phys. Rev. Lett.* **79**, 3178–3181.

Courant, R. & Hilbert, D. 1937 *Methods in Mathematical Physics*. Wiley & Sons.

Dowling, A. P. 1995 The calculation of thermoacoustic oscillations. *J. Sound Vib.* **180**, 557–581.

Dowling, A. P. 1997 Nonlinear self-excited oscillations of a ducted flame. *J. Fluid Mech.* **346**, 271–290.

Evesque, S. & Polifke, C. 2002 Low-order acoustic modelling for annular combustors: validation and inclusion of modal coupling. *ASME paper* gt-2002-30064.

Evesque, S., Polifke, C. & Pankiewitz, C. 2003 Spinning and azimuthally standing acoustic modes in annular combustors. *AIAA paper* 2003-3182.

George, J. & Sujith, R. I. 2009 Linear mechanism of wave emergence from vortices in smooth shear flows. *Phys. Rev.* E **79**, 046321-1–046321-6.

Golubev, V. V. & Atassi, H. M. 1998 Acoustic-vorticity waves in swirling flows. *J. Sound Vib.* **209**, 203–222.

Karimi, N., Brear, M. J. & Moase, W. H. 2008 Acoustic and disturbance energy analysis of a flow with heat communication. *J. Fluid Mech.* **597**, 67–89.

Kim, J. S. & Williams, F. A. 1998 Eigenmodes of acoustic pressure in combustion chambers. *J. Sound Vib.* **209**, 821–843.

Lamarque, N. & Poinsot, T. J. 2008 Boundary conditions for acoustic eigenmodes in gas turbine combustion chambers. *AIAA J.* **46**, 2282–2292.

Mani, R. 1981 Low-frequency sound propagation in a quasi-one-dimensional flow. *J. Fluid Mech.* **104**, 81–92.

Marble, F. E. & Candel, S. M. 1977 Gas non-uniformities convected through a nozzle. *J. Sound Vib.* **55**, 225–243.

Moase, W. H., Brear, M. J. & Manzie, C. 2007 The forced response of choked nozzles and supersonic diffusers. *J. Fluid Mech.* **585**, 281–304.

Rayleigh, J. W. S. 1896 *The Theory of Sound*. Macmillan.

Roux, S., Lartigue, G., Poinsot, T., Meier, U. & Berat, C. 2005 Studies of mean and unsteady flow in a swirled combustor using experiments, acoustic analysis and large eddy simulations. *Combust. Flame* **41**, 40–54.

https://doi.org/10.1017/S0022112010000261 Published online by Cambridge University Press

Saad, Y. & Martin, H. S. 1986 GMRES: a generalized minimal residual algorithm for solving nonsymmetric linear systems. *Sci. Comput. Stat.* **7** (3), 856–869.

Stow, S. R., Dowling, A. P. & Hynes, T. P. 2002 Reflection of circumferential modes in a choked nozzle. *J. Sound Vib.* **467**, 215–239.

Subrahmanyam, P. B., Sujith, R. I. & Lieuwen, T. C. 2001 A family of exact transient solutions for acoustic wave propagation in inhomogeneous, non-uniform area ducts. *J. Sound Vib.* **240** (4), 705–715.

Sujith, R. I., Waldherr, G. A. & Zinn, B. T. 1995 An exact solution for one-dimensional acoustic fields in ducts with an axial temperature gradient. *J. Sound Vib.* **184** (3), 389–402.

Tsien, H. S. 1952 The transfer functions of rocket nozzles. *Am. Rocket Soc. J.* **22**, 139–143.

Tyagi, M. & Sujith, R. 2003 Nonlinear distortion of travelling waves in variable-area ducts with entropy gradients. *J. Fluid Mech.* **492**, 1–22.

https://doi.org/10.1017/S0022112010000261 Published online by Cambridge University Press